RSC Advances

PAPER

View Article Online
View Journal | View Issue

Cite this: *RSC Adv.*, 2025, **15**, 10884

Synthesis of $Co_3Fe_7/CoFe_2O_4$ incorporated porous carbon catalysts *via* molten salt method: applications in the oxygen reduction reaction and 4-nitrophenol reduction†

Yanling Wu,[ab] Xi Tang,[a] Hui He,[a] Qingyuan Luo,[a] Wenkai Fu,[a] Qinggao Hou*[a] and Haijun Zhang*[c]

Received 7th February 2025
Accepted 1st April 2025

DOI: 10.1039/d5ra00893j

rsc.li/rsc-advances

Developing high-performance, multifunctional non-precious metal catalysts is essential for enhancing the efficiency of future energy utilization. In this study, four types of magnetic, recyclable $Co_3Fe_7/CoFe_2O_4$ incorporated porous carbon composite catalysts were synthesized using citric acid as the carbon source and ammonium chloride (NH_4Cl) as the salt medium. Iron and cobalt salts, in four different proportions, were uniformly incorporated using freeze-drying technology and subsequently processed through *in situ* calcination. Among the synthesized catalysts, $Co_3Fe_7/CoFe_2O_4$@NC-1, demonstrated outstanding catalytic reduction performance, with a reaction rate constant (k) of 0.031 min^{-1}, along with excellent cycle stability for 4-NP. The resulting $Co_3Fe_7/CoFe_2O_4$@NC-3 catalyst exhibited good ORR activity in an alkaline medium (E_{onset} = 0.99 V, $E_{1/2}$ = 0.83 V, J_L = −5.2 mA cm^{-2}), along with long-term durability and resistance to methanol poisoning. These hybrid materials hold promise as non-precious metal electrocatalysts for fuel cell ORRs and introduce a new class of catalytic candidates for 4-NP reduction.

1. Introduction

Designing eco-friendly catalyst materials is a key strategy for achieving green energy conversion and plays a crucial role in addressing global environmental and energy challenges.[1–3] The partially filled d-electron orbitals of precious metals make their surfaces highly receptive to adsorbing reactants, facilitating the formation of reaction intermediates. Noble metal catalysts exhibit outstanding catalytic activity and possess unique properties, including high-temperature tolerance, oxidation resistance, and corrosion resistance.[4] However, their widespread application is hindered by high costs, rapid deactivation, limited reusability, resource scarcity, and other drawbacks.[5,6] Transition metals are abundant and cost-effective, making them ideal candidates for developing efficient catalysts. Over the past few decades, metal-based nanomaterials, including metal oxides and alloys, have gained significant attention due to their crucial roles in physical and chemical interactions.[7–9] Transition metal catalysts demonstrate excellent thermal stability, strong resistance to toxins, extended lifespan, and enhanced selectivity in oxidation reactions. Similarly, the presence of oxygen vacancies increases the number of catalytic activation sites, further improving their performance.

Recently, there has been increasing interest in developing alternative catalysts that do not rely on precious metals. These include nanosized transition metals,[10] transition metal oxides,[11] nitrides,[12] chalcogenides,[13] and carbides.[14] Magnetic metal-based compounds, such as Co, Fe, and Ni,[15,16] have garnered significant attention due to their potential to overcome challenges related to catalyst recovery and reuse. As a result, various transition metal catalysts and their oxides, including Ni@NiO, CuO, NiO/NiS, CoO, $Co_3O_4/CoFe_2O_4$, and $CuFe_2O_4$/Ag, have been developed and utilized for the catalytic reduction of 4-nitrophenol (4-NP).[17–19] However, excessive clustering of magnetic metal nanoparticles (NPs) during synthesis adversely

[a]*School of Civil Engineering, Shandong Jiaotong University, Jinan 250357, China. E-mail: chqghou@163.com*

[b]*National United Engineering Laboratory for Biomedical Material Modification, Dezhou 251100, China*

[c]*Department of Vascular & Intervention, Tenth Peoples' Hospital of Tongji University, Shanghai 200072, China. E-mail: zhanghaijun@tongji.edu.cn*

† Electronic supplementary information (ESI) available: SEM images of the Co@NC, Fe/Fe_2O_3@NC, $Co_3Fe_7/CoFe_2O_4$@NC-2 and $Co_3Fe_7/CoFe_2O_4$@NC-4; PXRD patterns, Raman spectra, N_2 sorption isotherms, and the magnetic hysteresis loop at room temperature (T = 300 K) of the $Co_3Fe_7/CoFe_2O_4$@NC-2, $Co_3Fe_7/CoFe_2O_4$@NC-3, and $Co_3Fe_7/CoFe_2O_4$@NC-4; the high-resolution XPS spectra of C 1s, and O 1s core levels of $Co_3Fe_7/CoFe_2O_4$@NC-1 and $Co_3Fe_7/CoFe_2O_4$@NC-3 composite; LSV curves of $Co_3Fe_7/CoFe_2O_4$@NC-1, $Co_3Fe_7/CoFe_2O_4$@NC-2, $Co_3Fe_7/CoFe_2O_4$@NC-3, $Co_3Fe_7/CoFe_2O_4$@NC-4, $Co_3Fe_7/CoFe_2O_4$@NC-3-800, and $Co_3Fe_7/CoFe_2O_4$@NC-3-1000; amperometric i–t curves of $Co_3Fe_7/CoFe_2O_4$@NC-3 and 20 wt% Pt/C; SEM images of $Co_3Fe_7/CoFe_2O_4$@NC-3 catalyst after stability tests; PXRD patterns of $Co_3Fe_7/CoFe_2O_4$@NC-3 catalyst before and after stability tests; UV-vis absorption spectra of the reduction reaction systems in the presence of $Co_3Fe_7/CoFe_2O_4$@NC-2 and $Co_3Fe_7/CoFe_2O_4$@NC-4; cycling performances of the $Co_3Fe_7/CoFe_2O_4$@NC-3 catalyst. See DOI: https://doi.org/10.1039/d5ra00893j

affects their performance in practical applications. To prevent catalyst aggregation, these NPs are typically coupled with a carrier. Carbon-based carriers are particularly effective due to their ability to facilitate rapid electron transport, enhancing electron transfer between individual metal particles.[20–24] Common materials used for carbon carriers include polymers, graphene oxide (GO), and graphene. For example, Kong *et al.*[20] developed a thermal reduction synthesis technique to fabricate CoFe nanoparticles encapsulated within reduced graphene oxide (RGO) sheets *via* hydrogenation heat treatment. The resulting CoFe/RGO nanocomposite exhibited excellent catalytic efficiency for the reduction of 4-NP to 4-aminophenol (4-AP). Sun *et al.*[23] employed an electrospinning-assisted technique to produce one-dimensional carbon fibers containing MIL-53(Fe) as a precursor for fabricating carbon nanofiber (CNF)-based catalysts with enclosed Fe_3C or $CoFe_2O_4$ NPs. The aggregation and corrosion of $Fe_3C/CoFe_2O_4$ are minimized when encapsulated in carbon fibers during the oxygen reduction reaction (ORR) and oxygen evolution reaction (OER). Bai *et al.*[25] synthesized CoFe NPs by pyrolyzing metal and nitrogen/carbon-containing precursors, followed by their confinement within nitrogen-rich C_3N_4 nanosheets. ZIF-8 crystals were grown *in situ* on the surface of C_3N_4. This structure significantly enhances the graphitization of the carbon carrier during high-temperature treatment at 900 °C. Moreover, these NPs are specifically designed to prevent the agglomeration of alloy particles effectively. These studies highlight the diverse interactions between magnetic metal NPs and carbon-based auxiliary materials. The carbon component, particularly RGO, plays a crucial role in preventing particle aggregation and providing nucleation sites during synthesis.[26] However, the high cost of many carbon sources poses a significant barrier to their widespread industrial application. Therefore, identifying an affordable carbon source and developing a simple, efficient synthesis method for carbon-based nanocatalysts is essential.

In this study, four types of magnetic, recyclable $Co_3Fe_7/CoFe_2O_4$ incorporated porous carbon composite catalysts were synthesized using citric acid as a carbon source to inhibit the hydrolysis of metal salts and ammonium chloride as a salt medium to generate gas during high-temperature pyrolysis. Iron and cobalt salts, in four different proportions, were uniformly incorporated *via* freeze-drying and subsequently processed through *in situ* calcination. Among the synthesized catalysts, $Co_3Fe_7/CoFe_2O_4$@NC-1 demonstrated exceptional catalytic performance and strong cycling stability for the reduction of 4-NP. Furthermore, the $Co_3Fe_7/CoFe_2O_4$@NC-3 catalyst exhibited improved performance in the ORR under alkaline conditions, demonstrating excellent long-term stability and strong resistance to methanol poisoning. These hybrid materials hold potential for diverse applications and present a novel strategy for developing advanced catalysts.

2. Experimental section

2.1 Chemical and reagents

Ferrous chloride ($FeCl_2$, anhydrous), cobalt chloride ($CoCl_2$, anhydrous), citric acid ($C_6H_8O_7$), and NH_4Cl were purchased from Aladdin (Shanghai), while Nafion (5 wt%) and commercial platinum/carbon (20 wt% Pt/C) were obtained from Sigma-Aldrich Co. Ltd.

2.2 Synthesis of catalyst materials

First, a mixture of 6.0 g of NH_4Cl, 1.0 g of $C_6H_8O_7$, 0.2 g of $FeCl_2$, and 0.04 g of $CoCl_2$ was dissolved in 70 mL of deionized water and stirred for 2 hours until a homogeneous solution was achieved. Citric acid acted as both a carbon source and a hydrolysis inhibitor for the metal salts. The homogeneous solution was frozen at −50 °C and subsequently freeze-dried at −50 °C and 1.0 Pa. During this process, the ice in the precursor sublimated, yielding a uniform precursor powder. The obtained powder was then placed in a high-temperature tube furnace and calcined under an N_2 gas flow (50 mL min^{-1}) at 900 °C for 3 hours, with a heating rate of 3 °C min^{-1}. During calcination, the NH_4Cl template decomposed, releasing gas, while citric acid carbonized to form a porous carbon layer. The metal ions (Fe^{2+}, Co^{2+}) fused to form metal NPs, which were then dispersed on the porous carbon layers. Finally, the tube furnace was cooled to room temperature under an N_2 atmosphere, yielding the final sample, $Co_3Fe_7/CoFe_2O_4$@NC-3 (mole ratio 4 : 1). The Fe^{2+}/Co^{2+} molar ratios of 1 : 1, 2 : 1, 5 : 1, 0 : 3, and 3 : 0 were adjusted by varying the feed ratios of $FeCl_2$ and $CoCl_2$ while maintaining a total molar amount of 3 mmol. $Co_3Fe_7/CoFe_2O_4$@NC-1 (mole ratio 1 : 1), $Co_3Fe_7/CoFe_2O_4$@NC-2 (mole ratio 2 : 1), $Co_3Fe_7/CoFe_2O_4$@NC-4 (mole ratio 5 : 1), Co@NC (without $FeCl_2$), and Fe/Fe_2O_3@NC (without $CoCl_2$) were synthesized under identical conditions. To determine the optimal carbonization temperature, precursors with a mole ratio of 4 : 1 were also subjected to heat treatment at 800 °C and 1000 °C. Details regarding the characterization techniques and electrochemical measurements are provided in the ESI.†

2.3 Material characterization

Laboratory powder X-ray diffraction (XRD) patterns were recorded using a Rigaku Ultima IV diffractometer with a Cu Kα source (40 kV, 40 mA). The morphology and structure of the samples were examined using a field-emission scanning electron microscope (FE-SEM, Quant 250FEG) and a high-resolution transmission electron microscope (HR-TEM, JEM-2100F) operated at 200 kV. A Micromeritics Belsorp-max analyzer was employed to measure the Brunauer–Emmett–Teller (BET) surface area and pore size distribution (PSD). X-ray photoelectron spectroscopy (XPS) measurements were performed using a Kratos Axis Ultra instrument with monochromatic Al Kα radiation. Ultraviolet-visible (UV-vis) spectroscopy was conducted using a Hitachi U-4100 UV-vis spectrophotometer. Magnetic measurements were performed at room temperature with a vibrating sample magnetometer (VSM, LakeShore, USA, Model: 7404).

2.4 Electrochemical measurements

The electrochemical studies were conducted using a Gamry RDE710 electrochemical workstation with a three-electrode configuration. An Ag/AgCl (KCl-saturated) electrode served as

the reference electrode, while a carbon rod was used as the counter electrode. To ensure consistency, the working electrodes for all four catalysts were prepared using the same procedure. First, 5 mg of catalyst powder was dissolved in 0.8 mL of ethanol. Next, 40 μL of a 5 wt% Nafion solution (Sigma-Aldrich) was added, and the mixture was sonicated to achieve a uniform suspension. Finally, 10 μL of the resulting catalyst ink, with a concentration of 0.30 mg cm^{-2}, was applied to coat a glassy carbon electrode.

ORR studies were conducted using 0.1 M KOH electrolytes, saturated with nitrogen (N_2) or oxygen (O_2), at a scan rate of 50 mV s^{-1} applied to the electrodes. The ORR activity was measured using a rotating disk electrode (RDE) in an O_2-saturated 0.1 M KOH solution with linear sweep voltammetry (LSV) from 0.2 V to −0.8 V. Moreover, the ORR stability was assessed through chronoamperometric *i–t* tests at 1600 rpm in an O_2-saturated 0.1 M KOH solution over time. The performance of the developed catalysts was compared to that of a commercial Pt/C (20 wt%) electrocatalyst (HiSPEC3000, Alfa Aesar).

2.5 Catalytic reduction of 4-NP

To evaluate the catalytic properties, the reduction of 4-NP to 4-AP was investigated in the presence of sodium borohydride ($NaBH_4$). In the experiment, 2.7 mL of a 4-NP solution was mixed with 0.3 mL of a 0.1 M aqueous $NaBH_4$ solution, resulting in a yellowish hue in the final mixture. Subsequently, 5 mg of the hybrid catalyst was added to the solution. As no immediate color change was observed, it was inferred that the reaction proceeded at a very slow rate. The entire process was quantitatively monitored using a UV-visible spectrophotometer (Metash UV-6100). At regular intervals, 2.5 mL of the reaction solution was withdrawn and promptly analyzed using the UV-vis spectrophotometer. Measurements were conducted at room temperature within a scanning range of 250–500 nm.

3. Results and discussion

The preparation process for the $Co_3Fe_7/CoFe_2O_4$@NC-3 (mole ratio 4 : 1) catalyst is illustrated in Fig. 1. Initially, a homogeneous solution was obtained by dissolving NH_4Cl (6.0 g), citric acid ($C_6H_8O_7$, 1.0 g), $FeCl_2$ (1.23 mmol), and $CoCl_2$ (0.308 mmol) in 70 mL of deionized water, followed by continuous stirring for two hours. In this process, citric acid serves as both a carbon source and an acidifier, preventing the hydrolysis of the metal salts. The resulting homogeneous solution was then frozen at −50 °C and subsequently freeze-dried under vacuum conditions to obtain the precursor powder. During this process, NH_4Cl acted as a rigid template, effectively preventing the aggregation of citric acid and metal salts. Further, the carboxyl functional groups in citric acid strongly interacted with the metal ions, forming a uniform $FeCl_2$–$CoCl_2$–$C_6H_8O_7$ complex that coated the surface of the NH_4Cl template.[27] The precursor powder was then subjected to high-temperature calcination, during which NH_4Cl decomposed into gas and escaped, while citric acid carbonized to form a carbon layer. The metal ions fused to generate metal NPs, as illustrated in Fig. 1. $Co_3Fe_7/CoFe_2O_4$@NC-1 (mole ratio 1 : 1), $Co_3Fe_7/CoFe_2O_4$@NC-2 (mole ratio 2 : 1), and $Co_3Fe_7/CoFe_2O_4$@NC-4 (mole ratio 5 : 1), Co@NC (without $FeCl_2$), and Fe/Fe_2O_3@NC (without $CoCl_2$) were synthesized using same conditions for comparison.

3.1 Morphological and structural characterization

The electrocatalysts, $Co_3Fe_7/CoFe_2O_4$@NC-1 and $Co_3Fe_7/CoFe_2O_4$@NC-3 were initially examined using FE-SEM to investigate their morphological and structural characteristics. $Co_3Fe_7/CoFe_2O_4$@NC-1 displayed a complex three-dimensional structure with thick, curved plates (Fig. 2A). However, $Co_3Fe_7/CoFe_2O_4$@NC-3 exhibited a flat groove structure, with rice-like nanostructures faintly visible along the grooves (Fig. 2E). For a more detailed comparison, SEM images of Co@NC, Fe/Fe_2O_3@NC, $Co_3Fe_7/CoFe_2O_4$@NC-2, and $Co_3Fe_7/CoFe_2O_4$@NC-4 are provided in the ESI (Fig. S1–S3†). $Co_3Fe_7/CoFe_2O_4$@NC-1 and $Co_3Fe_7/CoFe_2O_4$@NC-3 morphology was further analyzed using TEM and HR-TEM, as shown in Fig. 2B–D, F and G. The TEM images of $Co_3Fe_7/CoFe_2O_4$@NC-1 and $Co_3Fe_7/CoFe_2O_4$@NC-3 clearly show fringe distances of 0.20 nm and 0.30 nm, corresponding to the (110) plane of the Co_3Fe_7 alloy[28] and the (220) plane of the $CoFe_2O_4$ spinel structure.[29,30] Furthermore, $Co_3Fe_7/CoFe_2O_4$@NC-1 and $Co_3Fe_7/CoFe_2O_4$@NC-3, exhibit a consistent horizontal band, identified as defective carbon with an interplanar distance of 0.34 nm, suggesting the presence of graphitic carbon.[31]

The XRD technique was used to evaluate the composition and phases of the synthesized $Co_3Fe_7/CoFe_2O_4$@NC-1, $Co_3Fe_7/CoFe_2O_4$@NC-2, $Co_3Fe_7/CoFe_2O_4$@NC-3, and $Co_3Fe_7/CoFe_2O_4$@NC-4 (Fig. 3A and S4†). The four composite catalysts exhibited similar peak patterns, corresponding to the Co_3Fe_7 phase at approximately 44.75° and 65.11° (JCPDS no. 48-1816),[32] and the $CoFe_2O_4$ phase at around 35.45°, 57.16°, and 62.72° (JCPDS no. 22-1086).[28] Moreover, slight shifts in the diffraction peaks (around 44.75° and 65.11°) suggest that increasing the iron content decreases the peak angles for the Co_3Fe_7 phase. This phenomenon can be attributed to the higher oxidation tendency of Fe^{2+} ions relative to Co^{2+} ions during the heating process, as shown in the ESI (Fig. S4†). Furthermore, the diffraction peak at approximately 26°, corresponding to the graphitized structure, shifted from a broad bulging shape to a sharp diffraction peak.[33]

Raman spectra of $Co_3Fe_7/CoFe_2O_4$@NC-1, $Co_3Fe_7/CoFe_2O_4$@NC-2, $Co_3Fe_7/CoFe_2O_4$@NC-3, and $Co_3Fe_7/CoFe_2O_4$@NC-4 showed two peaks at around 1330 cm^{-1} and 1590 cm^{-1} (Fig. 3B and S5†).[34,35] The order of I_D/I_G values is as follows: I_D/I_G ($Co_3Fe_7/CoFe_2O_4$@NC-1) = 1.12 > I_D/I_G ($Co_3Fe_7/CoFe_2O_4$@NC-2) = 1.09 > I_D/I_G ($Co_3Fe_7/CoFe_2O_4$@NC-3) = 1.07 > I_D/I_G ($Co_3Fe_7/CoFe_2O_4$@NC-4) = 1.03. Similarly, several weak signal peaks were detected in the high-wavelength region around 3000 cm^{-1}. The presence of these peaks, along with the high degree of graphitization, suggests a reduction in the charge transfer barrier.[36,37] Raman spectroscopy is widely regarded as an effective technique for identifying metal oxides. As shown in Fig. 3B, the $Co_3Fe_7/CoFe_2O_4$@NC-3 material exhibited weak peaks at approximately 181 ($T_{2g}(1)$), 304 (E_g), 463 ($T_{2g}(2)$), and 663

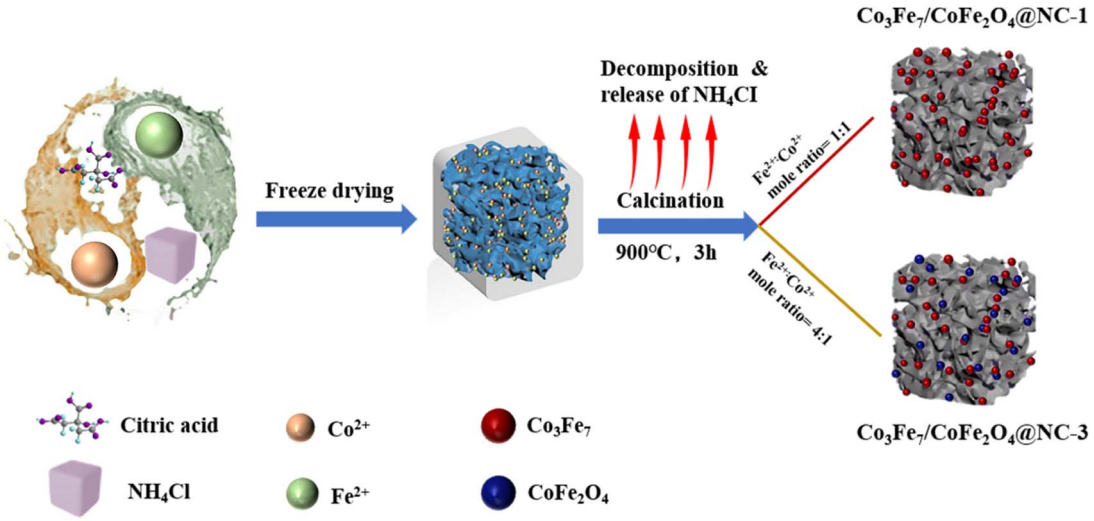

Fig. 1 Schematic illustration of the $Co_3Fe_7/CoFe_2O_4$@NC-1 and $Co_3Fe_7/CoFe_2O_4$@NC-3 nanocomposite formation.

($A_{1g}(1)$) cm^{-1}, which correspond to the characteristic peaks of the $CoFe_2O_4$ spinel.[28,38]

To precisely determine the surface areas of $Co_3Fe_7/CoFe_2O_4$@NC-1, $Co_3Fe_7/CoFe_2O_4$@NC-2, $Co_3Fe_7/CoFe_2O_4$@NC-3, and $Co_3Fe_7/CoFe_2O_4$@NC-4, nitrogen adsorption–desorption isotherms were measured (Fig. 3C, S6 and Table S1†). $Co_3Fe_7/CoFe_2O_4$@NC-3 exhibited a larger accessible surface area (517.58 $m^2\ g^{-1}$) compared to $Co_3Fe_7/CoFe_2O_4$@NC-1 (439.99 $m^2\ g^{-1}$), $Co_3Fe_7/CoFe_2O_4$@NC-2 (393.64 $m^2\ g^{-1}$), and $Co_3Fe_7/CoFe_2O_4$@NC-4 (447.37 $m^2\ g^{-1}$). The larger surface area of $Co_3Fe_7/CoFe_2O_4$@NC-3 enhances electrolyte infiltration and facilitates oxygen adsorption, thus improving its electrocatalytic performance.[39,40] Furthermore, all samples exhibited type IV isotherms with a hysteresis loop in the relative pressure (P/P^0) range of 0.45 to 0.99, indicating the presence and distribution of mesopores, as shown by the pore size distribution curves.[41,42]

The FeCo alloy is well known for its magnetic properties.[43,44] The magnetic behavior of the synthesized catalysts was evaluated using a vibrating sample magnetometer (Fig. 3D and S7†).[45] The magnetic behavior of micro-/nanosystems is influenced by factors such as particle size, shape, surface oxidation, and crystalline structure, with slight compositional changes significantly affecting saturation magnetization (M_s). The magnetic hysteresis loops of the catalysts, exhibiting typical ferromagnetic characteristics at 300 K, are shown in Fig. 3D and S7.† The $Co_3Fe_7/CoFe_2O_4$@NC-1 exhibited a slightly higher M_s (43.5 emu g^{-1}) compared to $Co_3Fe_7/CoFe_2O_4$@NC-2 (35.3 emu g^{-1}), $Co_3Fe_7/CoFe_2O_4$@NC-3 (35.7 emu g^{-1}), and $Co_3Fe_7/CoFe_2O_4$@NC-4 (35.4 emu g^{-1}).

The surface compositions and chemical states of $Co_3Fe_7/CoFe_2O_4$@NC-1 and $Co_3Fe_7/CoFe_2O_4$@NC-3 were analyzed using XPS (Fig. 4 and Table S2†). The survey spectra in Fig. 4A

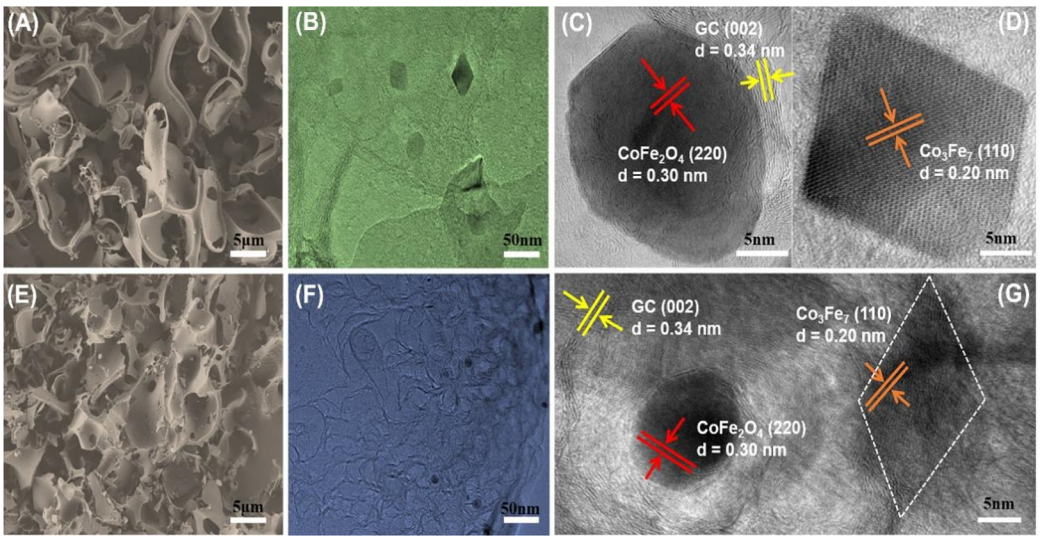

Fig. 2 Representative SEM (A and E), TEM (B and F), and lattice fringe HR-TEM (C, D and G) images of $Co_3Fe_7/CoFe_2O_4$@NC-1, and $Co_3Fe_7/CoFe_2O_4$@NC-3.

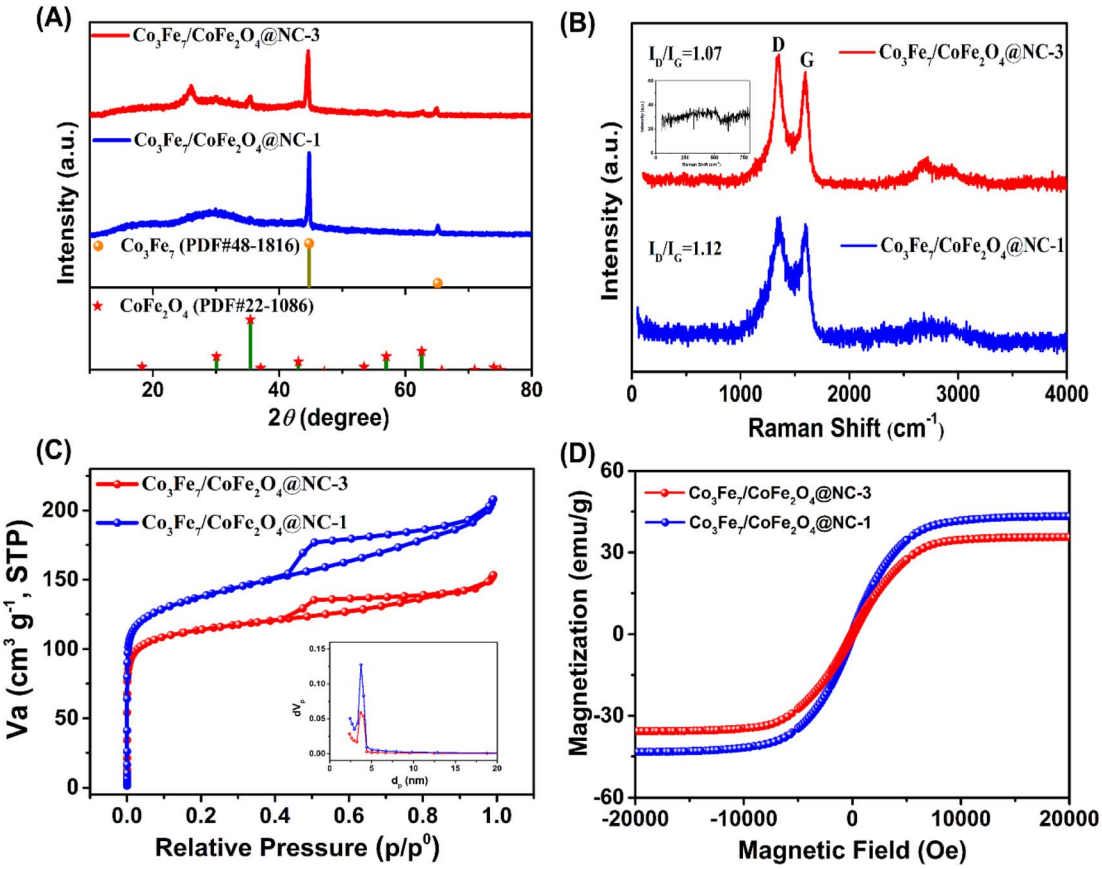

Fig. 3 (A) PXRD patterns; (B) Raman spectra; (C) N_2 sorption isotherms and BJH pore size distributions (inset); (D) the magnetic hysteresis loop at room temperature (T = 300 K) of $Co_3Fe_7/CoFe_2O_4$@NC-1 and $Co_3Fe_7/CoFe_2O_4$@NC-3.

show the presence of Co, Fe, C, N, and O elements. Fig. S8† demonstrates that the C 1s spectra display three main peaks corresponding to C–C, C–N, and O–C=O bonds.[46] Fig. 4B presents the high-resolution Co 2p spectra of $Co_3Fe_7/CoFe_2O_4$@NC-1 and $Co_3Fe_7/CoFe_2O_4$@NC-3. In the $Co_3Fe_7/CoFe_2O_4$@NC-1 sample, distinct peaks appear at 779.2 and 792.6 eV, 780.6 and 795.6 eV, 783.4 and 798.3 eV, and 786.9 and 803.6 eV, corresponding to zero-valence cobalt in the CoFe alloy, the Co–N_x bond, the ionic state of cobalt, and satellite peaks, respectively.[47,48] Fig. 4C presents the Fe 2p spectra of $Co_3Fe_7/CoFe_2O_4$@NC-1 and $Co_3Fe_7/CoFe_2O_4$@NC-3. For $Co_3Fe_7/CoFe_2O_4$@NC-1, the deconvoluted peaks appear at 709.1 and 720.0 eV (zero-valence Fe), 710.7 and 722.9 eV (Fe–N_x), 713.9 and 726.7 eV (Fe ions), and 717.2 and 732.1 eV (satellite peaks).[49] In $Co_3Fe_7/CoFe_2O_4$@NC-3, the zero-valence Co peak shifted to higher binding energies, appearing at 784.5 and 790.2 eV. Meanwhile, the Co peak exhibited a shift toward lower binding energies, indicating a transition to an ionic state, with the most pronounced shift at 782.1 and 797.9 eV. The zero-valence Fe binding energy decreased to 707.9 and 720.0 eV. This shift, along with the strong Co–Fe interaction, suggests electron transfer from Co to Fe. The core of the CoFe alloy undergoes charge redistribution, leading to enhanced surface energy. This modification facilitates oxygen species adsorption and desorption on the alloy NP surface, therefore improving the interfacial catalytic rate.[50] Fig. 4D presents the N 1s spectra of both samples, deconvoluted into pyridinic-N (398.3 eV), Co(Fe)–N_x (400.2 eV), pyrrolic-N (401.0 eV), and graphitic-N (402.3 eV).[51,52] The presence of M–N_x and other nitrogen-doping configurations indicates strong metal–nitrogen bonding and effective nitrogen incorporation into the carbon framework. $Co_3Fe_7/CoFe_2O_4$@NC-3 exhibited a higher pyridinic-N/graphitic-N ratio (2.78) than $Co_3Fe_7/CoFe_2O_4$@NC-1 (2.05). Pyridinic-N, with its lone-pair electrons, acts as an efficient catalytic site for the ORR.[53,54] Comparison of the XPS O 1s spectra revealed a single peak at 531.9 eV for $Co_3Fe_7/CoFe_2O_4$@NC-1, whereas $Co_3Fe_7/CoFe_2O_4$@NC-3 exhibited two peaks at 532.3 eV and 530.4 eV. The O1 peak, typically associated with low oxygen coordination at defect sites, appears in smaller particles. As shown in Fig. S9,† the presence of O_2 suggests metal–oxygen bonds, indicating Fe_2O_3 in the material.[25] The XPS data provide insights into the surface chemistry of $Co_3Fe_7/CoFe_2O_4$@NC-1 and $Co_3Fe_7/CoFe_2O_4$@NC-3, revealing the presence of pyridinic-N/graphitic-N, CoFe alloy, and various oxidation states of iron and cobalt. These surface characteristics are anticipated to play a crucial role in the material's electrochemical properties and catalytic performance.

3.2 Electrochemical properties for ORR

Cyclic voltammetry (CV) was conducted to assess the electrocatalytic ORR performance of the synthesized nanocomposites

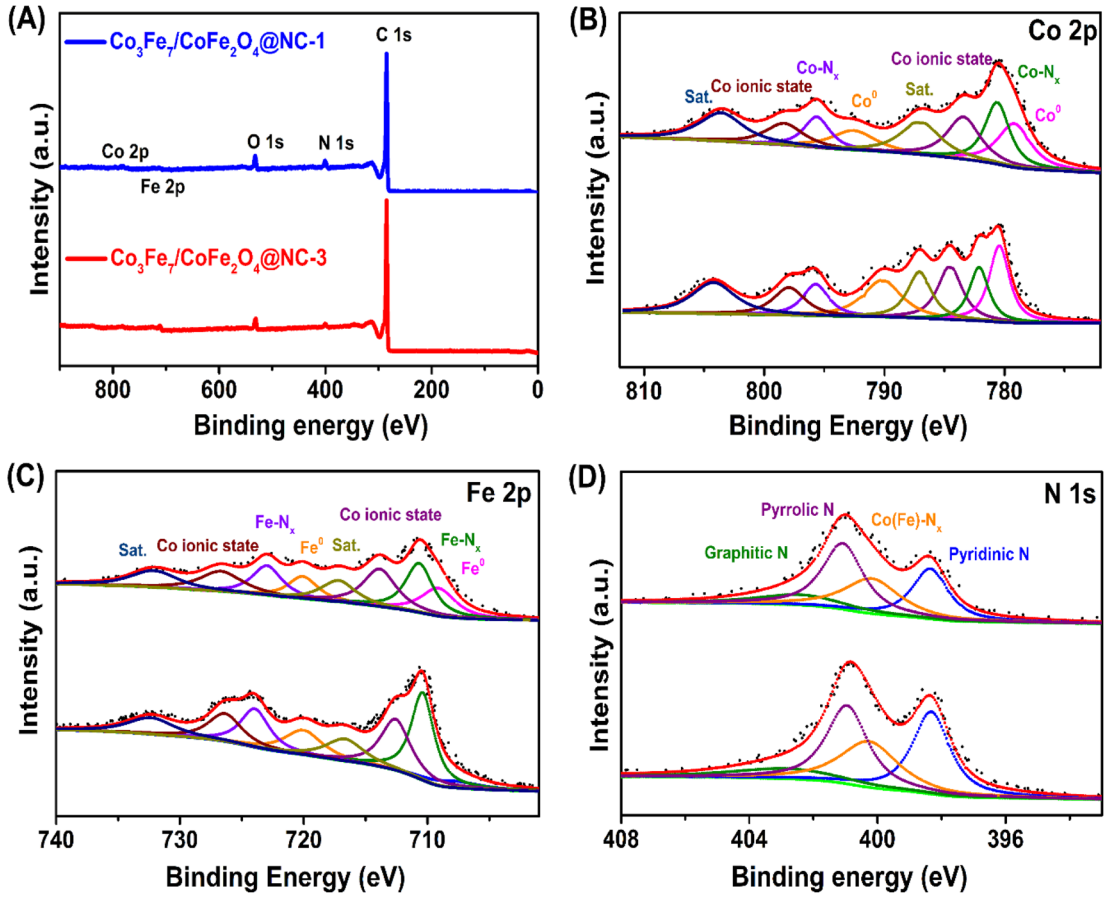

Fig. 4 XPS spectra of $Co_3Fe_7/CoFe_2O_4$@NC-1, and $Co_3Fe_7/CoFe_2O_4$@NC-3. (A) Survey spectra; (B) Co 2p; (C) Fe 2p; and (D) N 1s core levels.

in 0.1 M KOH under O_2- and N_2-saturated conditions at a scan rate of 50 mV s^{-1} (Fig. 5A and Table S3†). Among the four catalysts, $Co_3Fe_7/CoFe_2O_4$@NC-3 demonstrated the highest ORR activity, highlighting the significance of its active components in enhancing ORR catalysis.[55]

LSV polarization curves were used to assess ORR activity (Fig. 5B). Among all samples, $Co_3Fe_7/CoFe_2O_4$@NC-3 exhibited the highest performance (Fig. 5B, S10–S13 and Table S3†), with E_{onset} = 0.99 V, $E_{1/2}$ = 0.83 V, and J_L = −5.20 mA cm^{-2}. The activity followed the order: $Co_3Fe_7/CoFe_2O_4$@NC-2 (E_{onset} = 1.07 V, $E_{1/2}$ = 0.82 V, J_L = −5.80 mA cm^{-2}) > $Co_3Fe_7/CoFe_2O_4$@NC-4 (E_{onset} = 0.94 V, $E_{1/2}$ = 0.83 V, J_L = −5.61 mA cm^{-2}) > $Co_3Fe_7/CoFe_2O_4$@NC-1 (E_{onset} = 0.91 V, $E_{1/2}$ = 0.83 V, J_L = −3.29 mA cm^{-2}). These results highlight the significant impact of metal ratio adjustments on active catalyst composition and ORR performance. For comparison, CV and LSV profiles with the RDE configuration were used to evaluate the catalytic activities of $Co_3Fe_7/CoFe_2O_4$@NC-3 synthesized *via* pyrolysis at 800 °C and 1000 °C, denoted as $Co_3Fe_7/CoFe_2O_4$@NC-3-800 and $Co_3Fe_7/CoFe_2O_4$@NC-3-1000, respectively. The ORR activity of these samples was lower than that of $Co_3Fe_7/CoFe_2O_4$@NC-3, particularly at pyrolysis temperatures below or above 900 °C (Fig. 5B, S14, S15 and Table S3†). $Co_3Fe_7/CoFe_2O_4$@NC-3, pyrolyzed at 900 °C, exhibited high onset (0.99 V), half-wave (0.83 V), and limiting current densities (−5.20 mA cm^{-2}), comparable to the performance of commercial 20 wt% Pt/C.

The Tafel slope is expressed as follows:[56]

$$\text{Overpotential } g = a + b\log(j)$$

where j represents the current density, b denotes the Tafel slope, and a is constant. A lower b value indicates a smaller increase in overpotential with rising current density, suggesting faster reaction kinetics for the rate-determining step. In this study, the selected log(j) range considers a current density of 10 mA cm^{-2}, which serves as a benchmark for catalyst comparison.[57] The Tafel slope of $Co_3Fe_7/CoFe_2O_4$@NC-3 was 93 mV dec^{-1}, closely aligning with Pt/C (97 mV dec^{-1}) and $Co_3Fe_7/CoFe_2O_4$@NC-4 (109 mV dec^{-1}). However, $Co_3Fe_7/CoFe_2O_4$@NC-1 exhibited a lower value of 61 mV dec^{-1}, indicating distinct catalytic behavior, while $Co_3Fe_7/CoFe_2O_4$@NC-2 showed a significantly higher slope of 167 mV dec^{-1}, suggesting reduced ORR efficiency (Fig. 5C). Meanwhile, the LSV curves, recorded at various rotational speeds (400, 625, 900, 1225, 1600, 2025, and 2500 rpm) were used to investigate the ORR mechanism of the four nanocomposites (Fig. 5D). Based on the RDE test, the electron transfer number (n) was computed using the Koutechy–Levich (K–L) equations:[58]

$$1/J = 1/J_L + 1/J_K = 1/B\omega^{1/2} + 1/J_K \quad (1)$$

$$B = 0.62nFC_0(D_0)^{2/3}\nu^{-1\backslash 6} \quad (2)$$

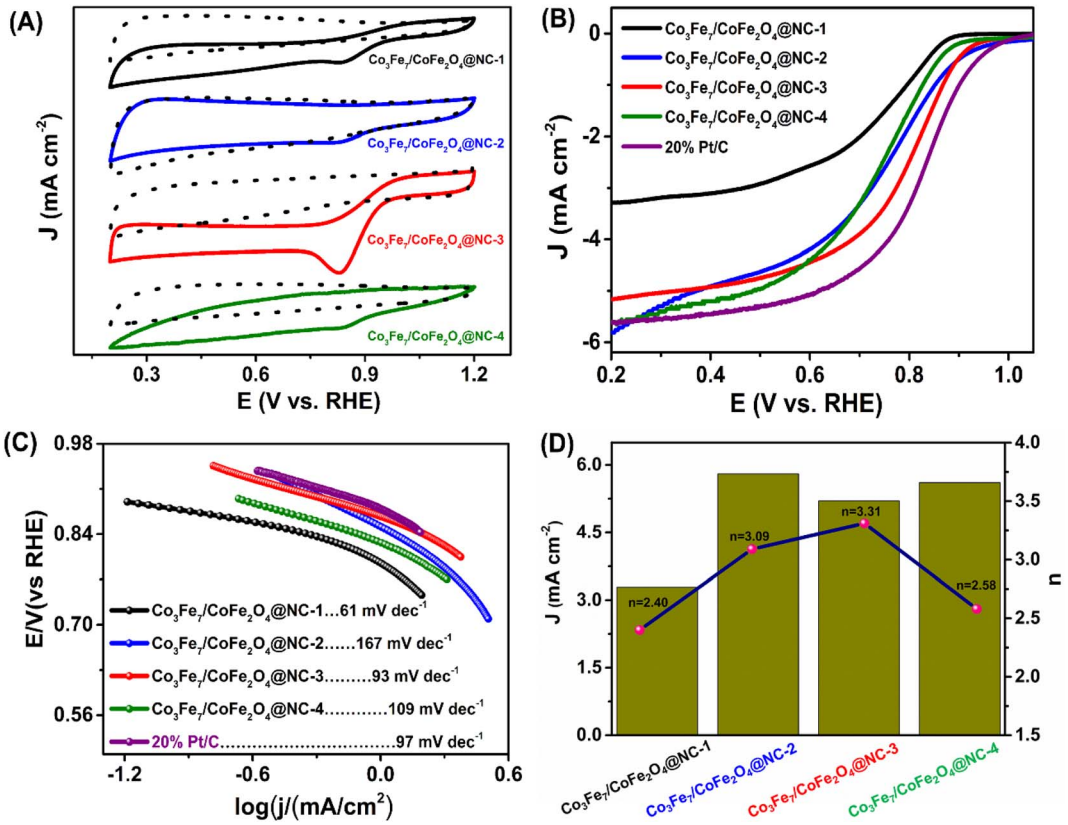

Fig. 5 (A) CV curves of $Co_3Fe_7/CoFe_2O_4$@NC-1, $Co_3Fe_7/CoFe_2O_4$@NC-2, $Co_3Fe_7/CoFe_2O_4$@NC-3, and $Co_3Fe_7/CoFe_2O_4$@NC-4 in a 0.1 M KOH solution (the solid lines represent O_2-saturated conditions, while the dotted lines represent N_2-saturated conditions). (B) LSV curves were obtained at 1600 rpm for the four produced nanocomposite samples and a commercial 20 wt% Pt/C catalyst in an oxygen-saturated 0.1 M KOH electrolyte. (C) Tafel graphs of the four synthesized nanocomposite samples and 20% Pt/C were generated using LSV data. (D) The limiting current density (J_L) and the electron transfer number (n) comparisons of $Co_3Fe_7/CoFe_2O_4$@NC-1, $Co_3Fe_7/CoFe_2O_4$@NC-2, $Co_3Fe_7/CoFe_2O_4$@NC-3, and $Co_3Fe_7/CoFe_2O_4$@NC-4.

$$J_K = nFkC_0 \quad (3)$$

In these equations, J represents the current density in the LSV curve, while J_L and J_K represent diffusion-limiting and kinetic-limiting current densities, respectively. B represents the reciprocal of the K–L curve slope, and ω represents the electrode rotation rate. C_0 (1.2×10^{-6} mol cm^{-3}) and D_0 (1.9×10^{-5} cm^2 s^{-1}) represent the bulk concentration and diffusion coefficient of oxygen in the 0.1 M KOH solution, respectively. F denotes the Faraday constant (96 485 C mol^{-1}), ν represents the dynamic viscosity and k represents the rate constant of electron transfer. The K–L plots exhibited excellent linearity from 0.4 V to 0.6 V *vs.* RHE, confirming first-order reaction kinetics for the ORR. The electron transfer number (n) for $Co_3Fe_7/CoFe_2O_4$@NC-3, determined from K–L analysis, was 3.31 (Fig. S12†), closely aligning with Pt/C (4.0). This suggests that $Co_3Fe_7/CoFe_2O_4$@NC-3 follows a four-electron ORR pathway for oxygen reduction.[59]

Long-term durability is crucial for assessing ORR catalyst performance. Stability tests for $Co_3Fe_7/CoFe_2O_4$@NC-3 and Pt/C in an oxygen-saturated 0.1 M KOH solution were conducted using time-amperometric measurements at 0.8 V and 1600 rpm. After 10 000 seconds, $Co_3Fe_7/CoFe_2O_4$@NC-3 retained 88% of its initial current density, whereas Pt/C retained only 60% (Fig. S16A†). The superior stability of $Co_3Fe_7/CoFe_2O_4$@NC-3 is attributed to its higher pyridinic-N content, which enhances Fe and Co anchoring, improving the dispersibility of active components on the carbon carrier.[60–62] The methanol crossover experiment confirmed the robust stability of $Co_3Fe_7/CoFe_2O_4$@NC-3, as its current density remained unchanged after methanol introduction. However, Pt/C exhibited a sharp decline due to methanol oxidation (Fig. S16B†). Cycling-accelerated durability testing was conducted to evaluate catalyst stability under alkaline conditions (Fig. S17†). After 10 000 CV cycles, the $E_{1/2}$ potential loss was 14 mV for $Co_3Fe_7/CoFe_2O_4$@NC-3 and 33 mV for Pt/C, confirming the improved stability of $Co_3Fe_7/CoFe_2O_4$@NC-3 compared to commercial Pt/C. The slight decrease in catalytic activity may be attributed to the partial growth of FeCo clusters in the spent catalyst, as evidenced by SEM analysis (Fig. S18†). The XRD patterns of $Co_3Fe_7/CoFe_2O_4$@NC-3 exhibited diffraction peaks similar to the original ones, confirming that its chemical composition remained unchanged after the durability test, demonstrating excellent electrochemical stability (Fig. S19†). These findings underscore the superior stability and methanol tolerance of $Co_3Fe_7/CoFe_2O_4$@NC-3 compared to Pt/C. Further, its catalytic efficiency surpassed that of previously reported iron oxide ORR catalysts (Table S4†).

3.3 Catalytic properties for 4-nitrophenol reduction

The reduction of aromatic nitro compounds to amines plays a vital role in organic synthesis and industrial production. Among these, 4-NP is a priority pollutant due to its high toxicity, carcinogenicity, and teratogenicity. Its conversion to 4-AP using sodium borohydride serves as a standard reaction for assessing the catalytic efficiency of metal or alloy catalysts.[63–65] Various catalysts have been explored for the degradation of 4-NP, including gold nanoparticles (AuNPs),[66] silver nanoparticles (AgNPs),[67] titanium dioxide (TiO_2), and[68] metal–organic frameworks (MOFs).[69] In this study, the catalytic performance of the synthesized nanocomposites was assessed *via* the reduction of 4-NP to 4-AP (Fig. 6). The reaction kinetics were examined using time-resolved spectra. As shown in Fig. 6A and B, the absorption peak of 4-NP at 400 nm decreased, while that of 4-AP at 300 nm increased, indicating successful conversion. The corresponding color change from yellow to colorless further confirmed the reaction.[19,20] For better comparison, the degradation of the other three composite catalysts ($Co_3Fe_7/CoFe_2O_4$@NC-2 and $Co_3Fe_7/CoFe_2O_4$@NC-4) was also performed (Fig. S20 and S21†).

This confirms the superior catalytic performance of $Co_3Fe_7/CoFe_2O_4$@NC-1 in 4-NP reduction. Pseudo-first-order kinetics was applied to determine kinetic parameters. The concentration ratio C_t/C_0 (where C_t and C_0 represent the concentrations of 4-NP at time t and 0, respectively) was calculated based on light absorption at 400 nm. The linear relationship between $\ln(C_t/C_0)$ and time (t) is shown in Fig. 6C, comparing the degradation efficiency of $Co_3Fe_7/CoFe_2O_4$@NC-1, $Co_3Fe_7/CoFe_2O_4$@NC-2, $Co_3Fe_7/CoFe_2O_4$@NC-3, and $Co_3Fe_7/CoFe_2O_4$@NC-4 catalysts. After 50 minutes, $Co_3Fe_7/CoFe_2O_4$@NC-1 achieved 79% degradation of 4-NP, followed by $Co_3Fe_7/CoFe_2O_4$@NC-4 (55%), $Co_3Fe_7/CoFe_2O_4$@NC-2 (42%), and $Co_3Fe_7/CoFe_2O_4$@NC-3 (28%). These results confirm $Co_3Fe_7/CoFe_2O_4$@NC-1 as the most efficient catalyst for 4-NP reduction.[70] The apparent rate constant k for the catalysts synthesized under different conditions was determined as follows: $k(Co_3Fe_7/CoFe_2O_4$@NC-1$) = 0.031\ min^{-1} > k(Co_3Fe_7/CoFe_2O_4$@NC-4$) = 0.017\ min^{-1} > k(Co_3Fe_7/CoFe_2O_4$@NC-2$) = 0.011\ min^{-1} > k(Co_3Fe_7/CoFe_2O_4$@NC-3$) = 0.006\ min^{-1}$. The highest k value of $0.031\ min^{-1}$ for $Co_3Fe_7/CoFe_2O_4$@NC-1 confirms its superior catalytic efficiency in the reduction of 4-NP.

To evaluate the reusability and stability of the synthesized catalysts, degradation experiments of 4-NP were conducted using $Co_3Fe_7/CoFe_2O_4$@NC-1 over five cycles. As shown in Fig. 6D, the k values and corresponding linear correlations were plotted. After five cycles, $Co_3Fe_7/CoFe_2O_4$@NC-1 exhibited only a 6% performance decrease, retaining over 70% of its initial catalytic activity and demonstrating excellent stability. For

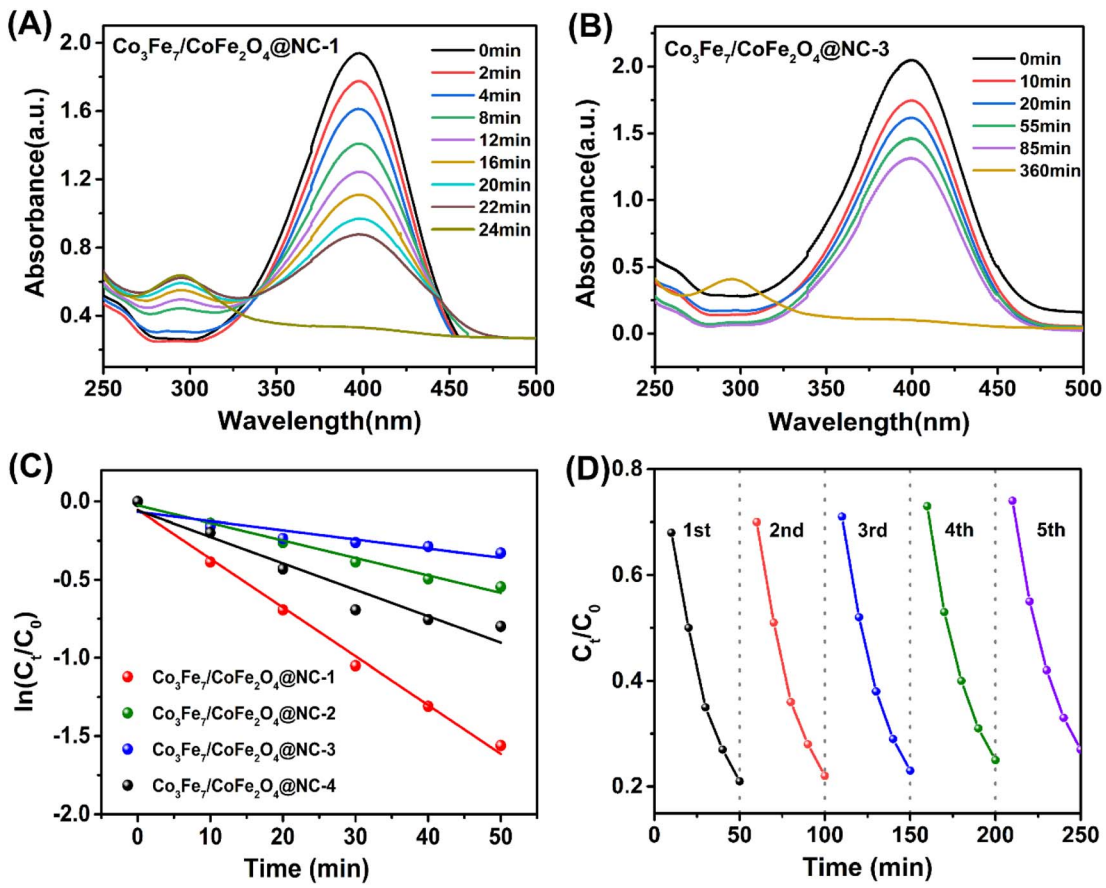

Fig. 6 The UV-vis absorption spectra of the reduction process were measured in the presence of (A) $Co_3Fe_7/CoFe_2O_4$@NC-1 and (B) $Co_3Fe_7/CoFe_2O_4$@NC-3. (C) The $\ln(C_t/C_0)$ plots compare the response times for the reduction of 4-NP catalyzed by $Co_3Fe_7/CoFe_2O_4$@NC-1, $Co_3Fe_7/CoFe_2O_4$@NC-2, $Co_3Fe_7/CoFe_2O_4$@NC-3, and $Co_3Fe_7/CoFe_2O_4$@NC-4. (D) Cycling performances of the $Co_3Fe_7/CoFe_2O_4$@NC-1.

comparison, the k values for $Co_3Fe_7/CoFe_2O_4$@NC-1, tested for reusability, are presented in Fig. S22,† showing a decline in stability and reusability. These findings underscore the superior catalytic efficiency and reusability of $Co_3Fe_7/CoFe_2O_4$@NC-1.

4. Conclusions

In summary, four composite catalyst materials ($Co_3Fe_7/CoFe_2O_4$@NC-1, $Co_3Fe_7/CoFe_2O_4$@NC-2, $Co_3Fe_7/CoFe_2O_4$@NC-3, and $Co_3Fe_7/CoFe_2O_4$@NC-4) were synthesized using the molten salt method. Among these, $Co_3Fe_7/CoFe_2O_4$@NC-1 exhibited superior catalytic reduction efficiency and maintained favorable durability over multiple cycles in 4-NP reduction. Meanwhile, $Co_3Fe_7/CoFe_2O_4$@NC-3 demonstrated excellent ORR performance in an alkaline environment, with improved stability and resistance to methanol-induced deactivation. The surface chemistry characteristics, including the proportion of pyridinic-N/graphitic-N, the oxidation states of cobalt and iron, and the presence of oxidized or/and unoxidized CoFe alloy, significantly influence the catalytic effectiveness and electrochemical properties of $Co_3Fe_7/CoFe_2O_4$@NC-1 and $Co_3Fe_7/CoFe_2O_4$@NC-3. Furthermore, all hybrid materials exhibited excellent ferromagnetic properties at ambient temperature, allowing for efficient manipulation by an external magnetic field. Their outstanding catalytic performance, ease of recyclability, and cost-effectiveness make these newly developed composite catalysts highly promising for applications in catalysis.

Data availability

The authors declare that the data supporting the findings of this study are available within the paper and its ESI.†

Author contributions

Writing—original draft and writing—review & editing, Y.-l. Wu; investigation, H. He; data curation, X. Tang and Q.-y. Luo; supervision, H.-j. Zhang; funding acquisition, Q.-g. Hou; resources, W.-k. Fu. All authors have read and agreed to the published version of the manuscript.

Conflicts of interest

There are no conflicts to declare.

Acknowledgements

This work is financially supported by the Natural Science Foundation of Shandong Province (ZR2023QB023 and ZR2021MB027), and the Transportation Technology Innovation Plan of Shandong Province (2024B112-02). The authors would like to thank MJEditor (**https://www.mjeditor.com**) for its linguistic assistance during the preparation of this manuscript.

References

1 H. C. Tu, Y. L. Hsiao, Y. D. Lin, Y. G. Lin, D. L. Liao and K. S. Ho, Multi-functional hydrogen- and oxygen-capturing FeCo-N-C catalyst with improved hydrogenation of nitroarenes and ORR activity, *Chem. Eng. J.*, 2024, **487**, 150623.

2 S. F. Fu, C. Z. Zhu, J. H. Song, D. Du and Y. H. Lin, Metal-organic framework-derived non-precious metal nanocatalysts for oxygen reduction reaction, *Adv. Energy Mater.*, 2017, **7**, 1700363.

3 S. H. Yin, J. Yang, Y. Han, G. Li, L. Y. Wan, Y. H. Chen, C. Chen, X. M. Qu, Y. X. Jiang and S. G. Sun, Construction of highly active metal-containing nanoparticles and FeCo-N_4 composite sites for the acidic oxygen reduction reaction, *Angew. Chem., Int. Ed.*, 2020, **59**, 21976–21979.

4 S. D. Bhoyate, J. Y. Kim, F. M. Souza, J. Lin, E. Lee, A. Kumar and R. K. Gupta, Science and engineering for non-noble-metal-based electrocatalysts to boost their ORR performance: A critical review, *Coord. Chem. Rev.*, 2023, **474**, 21854.

5 Y. Yang, Z. Y. Lun, G. L. Xia, M. N. He and Q. W. Chen, Non-precious alloy encapsulated in nitrogen-doped graphene layers derived from MOFs as an active and durable hydrogen evolution reaction catalyst, *Energy Environ. Sci.*, 2015, **8**, 3563–3571.

6 F. R. Yang, X. L. Zhu, B. N. Jia, J. B. Hao, Y. R. Ma, P. F. Lu and D. H. Li, Trifunctional electrocatalysts of single transition metal atom doped g-C_4N_3 with high performance for OER, ORR and HER, *Int. J. Hydrogen Energy*, 2024, **51**, 195–206.

7 L. Yan, P. P. Li, Q. Y. Zhu, A. Kumar, K. Sun, S. B. Tian and X. M. Sun, Atomically precise electrocatalysts for oxygen reduction reaction, *Chem*, 2023, **9**, 280–342.

8 Y. G. Zhao, D. P. A. Saseendran, C. Huang, C. A. Triana, W. R. Marks, H. Chen, H. Zhao and G. R. Patzke, Oxygen evolution/reduction reaction catalysts: From in situ monitoring and reaction mechanisms to rational design, *Chem. Rev.*, 2023, **123**(9), 6257–6358.

9 M. Zhu and C. Zhang, FeCo nanoalloys encapsulated in pod-like N-doped carbon nanotubes as efficient oxygen reduction reaction electrocatalysts for zinc-air batteries, *J. Alloys Compd.*, 2022, **921**, 166122.

10 L. Ma, S. Chen, Z. Pei, Y. Huang, G. Liang, F. Mo, Q. Yang, J. Su, Y. Gao, J. A. Zapien and C. Zhi, Single-Site Active Iron-Based Bifunctional Oxygen Catalyst for a Compressible and Rechargeable Zinc–Air Battery, *ACS Nano*, 2018, **12**, 1949–1958.

11 A. Aijaz, J. Masa, C. Rosler, W. Xia, P. Weide, A. J. R. Botz, A. Fischer, W. Schuhmann and M. Muhler, Angew. Chem. Co@Co_3O_4 encapsulated in carbon nanotube-grafted nitrogen-doped carbon polyhedra as an advanced bifunctional oxygen electrode, *Angew. Chem., Int. Ed.*, 2016, **55**, 4087–4091.

12 J. A. Varnell, E. C. Tse, C. E. Schulz, T. T. Fister, R. T. Haasch, J. A. Timoshenko, I. Frenkel and A. A. Gewirth, Identification of carbon-encapsulated iron nanoparticles as active species

in non-precious metal oxygen reduction catalysts, *Nat. Commun.*, 2016, **7**, 12582.

13 W. Xia, A. Mahmood, Z. Liang, R. Zou and S. Guo, Earth-abundant nanomaterials for oxygen reduction, *Angew. Chem., Int. Ed.*, 2016, **55**, 2650–2676.

14 W. X. Yang, X. J. Liu, X. Y. Yue, J. B. Jia and S. J. Guo, Bamboo-like carbon nanotube/Fe3C nanoparticle hybrids and their highly efficient catalysis for oxygen reduction, *J. Am. Chem. Soc.*, 2015, **137**, 1436–1439.

15 Z. J. Zhu, H. J. Yin, Y. Wang, C. H. Chuang, L. Xing, M. Y. Dong, Y. R. Lu, G. Casillas-Garcia, Y. Zheng, S. Chen, Y. Dou, P. Liu, Q. Cheng and H. Zhao, Coexisting single-atomic Fe and Ni sites on hierarchically ordered porous carbon as a highly efficient ORR electrocatalyst, *Adv. Mater.*, 2020, **32**, 2004670.

16 D. Zhou, Z. Cai, X. Lei, W. Tian, Y. Bi, Y. Jia, N. Han, T. Gao, Q. Zhang, Y. Kuang, J. Pan, X. Sun and X. Duan, NiCoFe-layered double hydroxides/N-doped graphene oxide array colloid composite as an efficient bifunctional catalyst for oxygen electrocatalytic reactions, *Adv. Energy Mater.*, 2018, **8**, 1701905.

17 Y. L. Zhao, B. Y. Cao, Z. Lin and X. T. Su, Synthesis of $CoFe_2O_4$/C nano-catalyst with excellent performance by molten salt method and its application in 4-nitrophenol reduction, *Environ. Pollut.*, 2019, **254**, 112961.

18 J. L. Ortiz-Quiñonez and U. Pal, Borohydride-assisted surface activation of Co_3O_4/$CoFe_2O_4$ composite and its catalytic activity for 4-nitrophenol reduction, *ACS Omega*, 2019, **4**, 10129–10139.

19 C. Hou, D. Y. Zhao, W. Q. Chen, H. Li, S. F. Zhang and C. Liang, Covalent organic framework-functionalized magnetic $CuFe_2O_4$/Ag nanoparticles for the reduction of 4-nitrophenol, *Nanomaterials*, 2020, **10**, 426.

20 C. C. Kong, W. J. Lei, B. S. Lei, F. Z. Pu, G. Wang, X. J. Zhang, C. Zhou and Z. M. Yang, CoFe nanoparticle-decorated reduced graphene oxide for the highly efficient reduction of 4-nitrophenol, *Langmuir*, 2021, **37**, 10987–10993.

21 Y. Wu, W. Pan, Y. Li, B. Yang, B. Meng, R. Li and R. Yu, Surface-oxidized amorphous Fe nanoparticles supported on reduced graphene oxide sheets for microwave absorption, *ACS Appl. Nano Mater.*, 2019, **2**, 4367–4376.

22 H. Zhu, A. Guo, L. Xian, Y. Wang, Y. Long and G. Y. Fan, Facile fabrication of surface vulcanized Co-Fe spinel oxide nanoparticles toward efficient 4-nitrophenol destruction, *J. Hazard. Mater.*, 2022, **430**, 128433.

23 Y. B. Sun, Y. Li, S. J. You, X. R. Li, Y. Zhang, Z. Cai, M. Y. Liu, N. Q. Ren and J. L. Zou, Fe_3C/$CoFe_2O_4$ nanoparticles wrapped in one-dimensional MIL-53 (Fe)-derived carbon nanofibers as efficient dual-function oxygen catalysts, *Chem. Eng. J.*, 2021, **424**, 130460.

24 L. B. Ma, X. P. Shen, G. X. Zhu, Z. Y. Ji and H. Zhou, FeCo nanocrystals encapsulated in N-doped carbon nanospheres/thermal reduced graphene oxide hybrids: Facile synthesis, magnetic and catalytic properties, *Carbon*, 2014, **77**, 255–265.

25 J. R. Bai, L. Cheng, S. X. Liu, Y. B. Lian, Y. Y. Deng, Q. F. Zhou, M. Xiang, Y. W. Tang and Y. Q. Su, Construct N-doped carbon anchored CoFe alloy nanoparticles with high content graphitic-N for electrocatalytic oxygen reduction, *J. Colloid Interface Sci.*, 2024, **653**, 1785–1791.

26 X. T. Liu, M. Z. Huang, S. T. Yang, R. Devasenathipathy, L. H. Xie, Z. Y. Yang, L. M. Wang, D. J. Huang, X. L. Peng and D. H. Chen, Spatially confined radical addition reaction for electrochemical synthesis of carboxylated graphene and its applications in water desalinationand splitting, *Small*, 2024, **20**, 2401972.

27 P. B. Zhai, L. X. Liu, Y. Wei, J. H. Zuo, Z. L. Yang, Q. Chen, F. F. Zhao, X. K. Zhang and Y. J. Gong, Self-healing nucleation seeds induced long-term dendrite-free lithium metal anode, *Nano Lett.*, 2021, **21**, 7715–7723.

28 Y. B. Zhou, Y. L. Zhang and X. M. Hu, Synergistic coupling Co_3Fe_7 alloy and $CoFe_2O_4$ spinel for highly efficient removal of 2,4-dichlorophenol by activating peroxymonosulfate, *Chemosphere*, 2020, **242**, 125244.

29 M. L. Tan, T. He, J. Liu, H. Q. Wu, Q. Li, J. Zheng, Y. Wang, Z. F. Sun, S. Y. Wang and Y. Zhang, Supramolecular bimetallogels: A nanofiber network for bimetal/nitrogen co-doped carbon electrocatalysts, *J. Mater. Chem. A*, 2018, **6**, 8227–8232.

30 X. Wang, L. Z. Zhuang, Y. Jia, L. J. Zhang, Q. Yang, W. J. Xu, D. J. Yang, X. C. Yan, L. Z. Zhang, Z. H. Zhu, C. L. Brown, P. Yuan and X. D. Yao, One-step in-situ synthesis of vacancy-rich $CoFe_2O_4$@defective graphene hybrids as bifunctional oxygen electrocatalysts for rechargeable Zn-Air batteries, *Chem. Res. Chin. Univ.*, 2020, **36**, 479–487.

31 X. Q. Xu, J. H. Xie, B. Liu, R. Y. Wang, M. Y. Liu, J. Zhang, J. Liu and Z. Cai, PBA-derived FeCo alloy with core-shell structure embedded in 2D N-doped ultrathin carbon sheets as a bifunctional catalyst for rechargeable Zn-air batteries, *Appl. Catal., B*, 2022, **316**, 121687.

32 Y. M. Ma, L. Gan, D. Li, Y. Y. Gao, X. X. Yang, K. Wang, S. Y. Lu, H. Wu, S. J. Ding and C. H. Xiao, Rational modulation of N, P co-doped carbon nanotubes encapsulating Co_3Fe_7 alloy as bifunctional oxygen electrocatalysts for Zinc–Air batteries, *J. Power Sources*, 2019, **441**, 227177.

33 W. Yan, Y. L. Wu, Y. L. Chen, Q. Liu, K. Wang, N. Cao, F. N. Dai and X. Y. Li, Facile preparation of N-doped corncob-derived carbon nanofiber efficiently encapsulating Fe_2O_3 nanocrystals towards high ORR electrocatalytic activity, *J. Energy Chem.*, 2020, **44**, 121–130.

34 Y. Deng, Y. Dong, G. Wang, K. Sun, X. Shi, L. Zheng, X. Li and S. Liao, Well-defined ZIF-derived Fe-N codoped carbon nanoframes as efficient oxygen reduction catalysts, *ACS Appl. Mater. Interfaces*, 2017, **9**, 9699–9709.

35 Y. L. Wu, Z. X. Xiao, Z. C. Jin, X. L. Li and Y. L. Chen, The cobalt carbide/bimetallic CoFe phosphide dispersed on carbon nanospheres as advanced bifunctional electrocatalysts for the ORR, OER, and rechargeable Zn–air batteries, *J. Colloid Interface Sci.*, 2021, **590**, 321–329.

36 Y. H. Zeng, C. Z. Li, B. Y. Li, J. S. Liang, J. M. Zachman, D. A. Cullen, R. P. Hermann, A. E. Ercan, B. Lavina, S. Karakalos, M. Lucero, B. Z. Zhang, M. Y. Wang, Z. X. Feng, G. F. Wang, J. Xie, D. J. Myers, J. P. Dodelet and

G. Wu, Tuning the thermal activation atmosphere breaks the activity–stability trade-off of Fe–N–C oxygen reduction fuel cell catalysts, *Nat. Catal.*, 2023, **6**, 1215–1227.

37 C. Li, Z. Chen, Y. Ni, A. Kong and Y. Shan, Coordination compound-derived ordered mesoporous N-free Fe–Px–C material for efficient oxygen electroreduction, *J. Mater. Chem. A*, 2016, **4**, 14291–14297.

38 X. Y. Lv, M. Yu, Y. L. Guo and M. H. Sui, Efficient heterogeneous activation of peroxymonosulfate by Ag-doped $CoFe_2O_4$ nanoparticles for sulfamethoxazole degradation, *J. Environ. Chem. Eng.*, 2023, **11**, 110980.

39 Y. L. Eu, Y. L. Chen, H. Q. Wang, C. M. Wang, A. S. Wang, S. Zhao, X. Y. Li, D. F. Sun and J. Z. Jiang, Efficient ORR electrocatalytic activity of peanut shell-based graphitic carbon microstructures, *J. Mater. Chem. A*, 2018, **6**, 12018–12028.

40 Z. P. Zhang, J. T. Sun, F. Wang and L. M. Dai, Efficient oxygen reduction reaction (ORR) catalysts based on single iron atoms dispersed on a hierarchically structured porous carbon framework, *Angew. Chem., Int. Ed.*, 2018, **57**, 9038–9043.

41 Y. Wang, Y. Pan, L. K. Zhu, H. H. Yu, B. Y. Duan, R. W. Wang, Z. T. Zhang and S. Y. Qiu, Solvent-free assembly of Co/Fe-containing MOFs derived N-doped mesoporous carbon nanosheets for ORR and HER, *Carbon*, 2019, **146**, 671–679.

42 H. W. Liang, W. Wei, Z. S. Wu, X. L. Feng and K. Müllen, Mesoporous metal–nitrogen-doped carbon electrocatalysts for highly efficient oxygen reduction reaction, *J. Am. Chem. Soc.*, 2013, **135**(43), 16002–16005.

43 P. Karipoth, A. Thirumurugan, S. Velaga, J. M. Greneche and R. J. Joseyphus, Magnetic properties of FeCo alloy nanoparticles synthesized through instant chemical reduction, *J. Appl. Phys.*, 2016, **120**, 123906.

44 H. Can, K. Icin, S. Akyol, U. Topal, S. Öztürk and H. Sözeri, The magnetic field sensing performance of FeCo-based soft magnetic alloys with varying Fe/Co ratio, *J. Alloys Compd.*, 2023, **966**, 171515.

45 T. D. Trang, T. C. Khiem, E. Kwon, J.-C. Wen, X. G. Duan, H. M. Bui, C. C. Hu, Y. F. Tsang, W.-H. Chen and K.-Y. A. Lin, Interface-engineered hollow carbon matrix-supported FeCo alloy as an enhanced magnetic activator for peroxymonosulfate to degrade an endocrine disruptor in water: A comparative study for elucidating advantageous roles of Fe-dopant, *Surf. Interfaces*, 2023, **42**, 103338.

46 S. Q. Guo, Y. X. Sun, J. N. Wang, L. C. Peng, H. Y. Li and C. J. Li, Bimetallic ZIF-derived cobalt nanoparticles anchored on N- and S-codoped porous carbon nanofibers as cathode catalyst for Li-O_2 batteries, *Electrochim. Acta*, 2022, **418**, 140279.

47 S. Q. Guo, S. Y. Yu, F. Chen, L. Wang, M. Guo, T. L. Ren, C. Zhang and C. J. Li, Direct methanol fuel cell with enhanced oxygen reduction performance enabled by CoFe alloys embedded into N-doped carbon nanofiber and bamboo-like carbon nanotube, *J. Colloid Interface Sci.*, 2023, **652**, 429–439.

48 F. F. Fan, Q. L. Huang, K. K. Rani, X. L. Peng, X. T. Liu, L. M. Wang, Z. Y. Yang, D. J. Huang, R. Devasenathipathy, D. H. Chen, Y. J. Fan and W. Chen, Interface and doping engineering of Co-based electrocatalysts for enhanced oxygen reduction and evolution reactions, *Chem. Eng. J.*, 2023, **470**, 144380.

49 Y. Liu, X. Wu, X. Guo, K. Lee, Q. Sun, X. Li, B. Zhang, Z. Wang, J. Hu, Y. Zhu, M. K. H. Leung and Z. Zhu, Modulated FeCo nanoparticle in situ growth on the carbon matrix for high-performance oxygen catalysts, *Mater. Today Energy*, 2021, **19**, 100610.

50 C. Deng, J. J. Tan, C. Y. Toe, X. Li, G. D. Li, X. X. Jiang, S. M. Wei, H. P. Yang, Q. Hu and C. X. He, Achieving efficient oxygen reduction on ultra-low metal-loaded electrocatalysts by constructing well-dispersed bimetallic sites and interconnected porous channels, *J. Mater. Chem. A*, 2022, **10**, 17217–17224.

51 L. Zhou, P. Zhou, Y. L. Zhang, B. Y. Liu, P. Gao and S. J. Guo, 3D star-like atypical hybrid MOF derived single-atom catalyst boosts oxygen reduction catalysis, *J. Energy Chem.*, 2021, **55**, 355–360.

52 Y. Q. Jing, Y. Y. Cheng, L. Wang, Y. Liu, B. H. Yu and C. Yang, MOF-derived Co, Fe, and Ni codoped N-enriched hollow carbon as efficient electrocatalyst for oxygen reduction reaction, *Chem. Eng. J.*, 2020, **397**, 125539.

53 X. Hu, Y. Min, L.-L. Ma, J.-Y. Lu, H.-C. Li, W.-J. Liu, J.-J. Chen and H.-Q. Yu, Ironnitrogen doped carbon with exclusive presence of FexN active sites as an efficient ORR electrocatalyst for Zn-air battery, *Appl. Catal., B*, 2020, **268**, 118405.

54 L. Lin, Q. Zhu and A. W. Xu, Noble-metal-free Fe-N/C catalyst for highly efficient oxygen reduction reaction under both alkaline and acidic conditions, *J. Am. Chem. Soc.*, 2014, **136**, 11027–11033.

55 X. Q. Huang, X. J. Wu, Y. L. Niu, C. L. Dai, M. W. Xu and W. H. Hu, Effect of nanoparticle composition on oxygen reduction reaction activity of Fe/N–C catalysts: a comparative study, *Catal. Sci. Technol.*, 2019, **9**, 711–717.

56 G. Li, L. Anderson, Y. Chen, M. Pan and P. Y. Abel Chuang, New insights into evaluating catalyst activity and stability for oxygen evolution reactions in alkaline media, *Sustainable Energy Fuels*, 2018, **2**, 237–251, DOI: **10.1039/C7SE00337D**.

57 G. A. Gebreslasea, M. V. Martínez-Huertab, D. Sebastiána and M. J. Lázaro, Transformation of $CoFe_2O_4$ spinel structure into active and robust CoFe alloy/N-doped carbon electrocatalyst for oxygen evolution reaction, *J. Colloid Interface Sci.*, 2022, **625**, 70–82.

58 J. Zhang, Y. Xie, Q. K. Jiang, S. Guo, J. H. Huang, L. L. Xu, Y. Wang and G. Li, Effect of nanoparticle composition on oxygen reduction reaction activity of Fe/N–C catalysts: a comparative study, *J. Mater. Chem. A*, 2022, **10**, 16920.

59 D. W. Wang and D. S. Su, Facile synthesis of cobalt cluster-CoNx composites: synergistic effect boosts electrochemical oxygen reduction, *Energy Environ. Sci.*, 2014, **7**, 576–591.

60 Y. Tong, P. Z. Chen, T. P. Zhou, K. Xu, W. S. Chu, C. Z. Wu and Y. Xie, A bifunctional hybrid electrocatalyst for oxygen reduction and evolution: Cobalt oxide nanoparticles strongly coupled to B, N-decorated graphene, *Angew. Chem., Int. Ed.*, 2017, **56**, 7121–7125.

61 W. Chaikittisilp, N. L. Torad, C. L. Li, M. Imura, N. Suzuki, S. Ishihara, K. Ariga and Y. Yamauchi, Synthesis of nanoporous carbon-cobalt-oxide hybrid electrocatalysts by thermal conversion of metal-organic frameworks, *Chem.—Eur. J.*, 2014, **20**, 4217–4221.

62 B. H. Zhang, M. Y. Le, J. Chen, H. Z. Guo, J. J. Wu and L. Wang, Enhancing defects of N-doped carbon nanospheres via ultralow Co atom loading engineering for a high-efficiency oxygen reduction reaction, *ACS Appl. Energy Mater.*, 2021, **4**, 3439–3447.

63 N. K. R. Bogireddy, Y. R. Mejia, T. M. Aminabhavi, V. Barba, R. H. Becerra, A. D. A. Flores and V. Agarwal, The identification of byproducts from the catalytic reduction reaction of 4-nitrophenol to 4-aminophenol: A systematic spectroscopic study, *J. Environ. Manage.*, 2022, **316**(2022), 115292.

64 S. S. Satapathy, P. Bhol, A. Chakkarambath, J. Mohanta, K. Samantaray, S. K. Bhat, S. K. Panda, P. S. Mohanty and S. Si, Thermo-responsive PNIPAM-metal hybrids: An efficient nanocatalyst for the reduction of 4-nitrophenol, *Appl. Surf. Sci.*, 2017, **420**, 753–763.

65 K. Wang, X. Zhu, Y. Yang, D. D. Ye, R. Chen and Q. Liao, Photothermal Reduction of 4-Nitrophenol to 4-Aminophenol Using Silver/Polydopamine Catalysts, *J. Environ. Chem. Eng.*, 2022, **10**, 108253.

66 M. T. Islam, H. Jing, T. Yang, E. Zubia, A. G. Goos, R. A. Bernal, C. E. Botez, M. Narayan, C. K. Chan and J. C. Noveron, Fullerene stabilized gold nanoparticles supported on titanium dioxide for enhanced photocatalytic degradation of methyl orange and catalytic reduction of 4-nitrophenol, *J. Environ. Chem. Eng.*, 2018, **6**, 3827–3836.

67 A. M. Mostafa, E. A. Mwafy, N. S. Awwad and H. A. Ibrahium, Synthesis of multi-walled carbon nanotubes decorated with silver metallic nanoparticles as a catalytic degradable material via pulsed laser ablation in liquid media, *Colloids Surf., A*, 2021, **626**, 126992.

68 A. B. Migdadi, Q. M. Al-Bataineh, A. A. Ahmad, H. M. Al-Khateeb and A. Telfah, Titanium dioxide/reduced graphene oxide nanocomposites as effective photocatalytic for hazardous 4-nitrophenol, *J. Alloys Compd.*, 2024, **971**, 172794.

69 M. E. Farshchi, N. M. Bozorg, A. Ehsani, H. Aghdasinia, Z. Chen, S. Rostamnia and B. J. Ni, Green valorization of PET waste into functionalized Cu-MOF tailored to catalytic reduction of 4-nitrophenol, *J. Environ. Manage.*, 2023, **345**, 118842.

70 J. Feng, L. Su, Y. H. Ma, C. L. Ren, Q. Guo and X. G. Chen, $CuFe_2O_4$ magnetic nanoparticles: A simple and efficient catalyst for the reduction of nitrophenol, *Chem. Eng. J.*, 2013, **221**, 16–24.